Supplementary Information

3D printed inks of two-dimensional semimetallic MoS_2/TiS_2 nanosheets for conductive-additive-free symmetric supercapacitors

*A. Panagiotopoulos[1], G. Nagaraju [1], S. Tagliaferri[1], C. Grotta[1], P. Sherrell[1+], M. Sokolikova[1], G. Cheng[1], F. Iacoviello[2], K. Sharda[1], C. Mattevi[1]**

[1] Department of Materials, Imperial College London, Exhibition Road, SW7 2AZ London, UK

[2] Electrochemical Innovation Lab, Department of Chemical Engineering, University College London, London WC1E 7JE, U.K

+ current affiliation Department of Chemical Engineering, The University of Melbourne, Parkville, Victoria 3010, Australia

** c.mattevi@imperial.ac.uk*

Two-step intercalation-exfoliation formulation for TMD ink blends:

The formulation is comprised of a two-step lithium (Li) intercalation mechanism and direct water exfoliation process followed by 3D printing of TMDs based electrodes suspended in a carrier hydrogel environment. These are schematically presented in the Figure (a-f). Bulk TMD powders (MoS_2 and TIS_2) were mixed with $LiBH_4$ for lithium (Li) intercalation. This is an established method to produce lithiated TMD compounds[1,2]. The Li intercalation process can be expressed (1) as below.

$$MS_2\ (MoS_2 \text{ or } TiS_2) + LiBH_4 \rightarrow LiMS_2 + B_2H_6\uparrow + H_2\uparrow \quad (1)$$

Firstly, the thermodynamically stable 2H MoS_2 was converted into 1T' $LiMoS_2$ while TiS_2 is inherently 1T and is lithiated[3]. Then, the intercalated powders are subsequently directly exfoliated with the poloaxomer hydrogel that acts both as the exfoliation initiator with the lithiated TMD powders but also as the carrier hydrogel for the additive manufacturing of the TMD blends. The exfoliation reaction is expressed below[4]:

$$LiMS_2 + H2O \rightarrow MS_2 + LiOH + H_2\uparrow \quad (2)$$

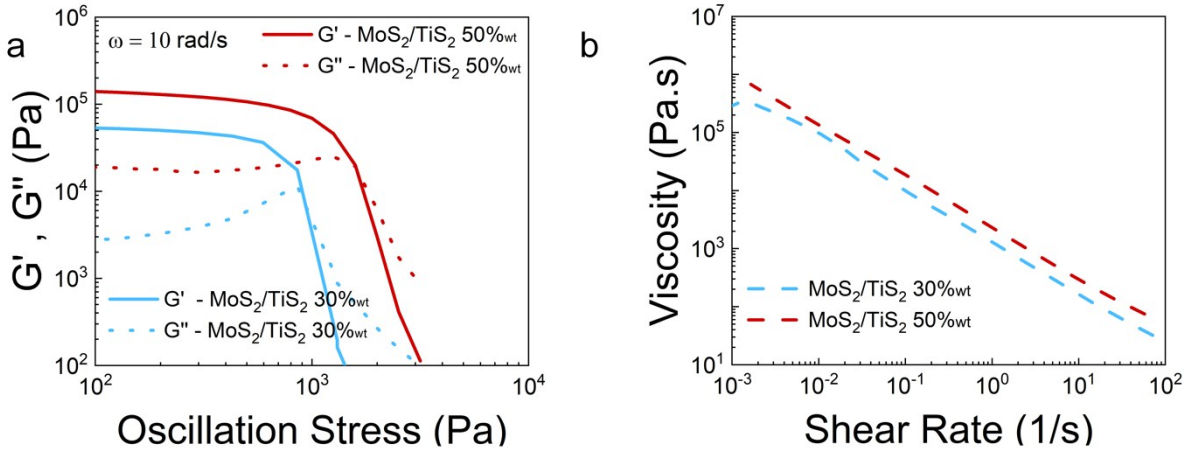

Figure S1. a) Oscillatory tests of MoS_2/TiS_2 inks in 30%wt (blue) and 50%wt (red). b) Flow ramps of MoS_2/TiS_2 inks in 30%wt (blue) and 50%wt (red).

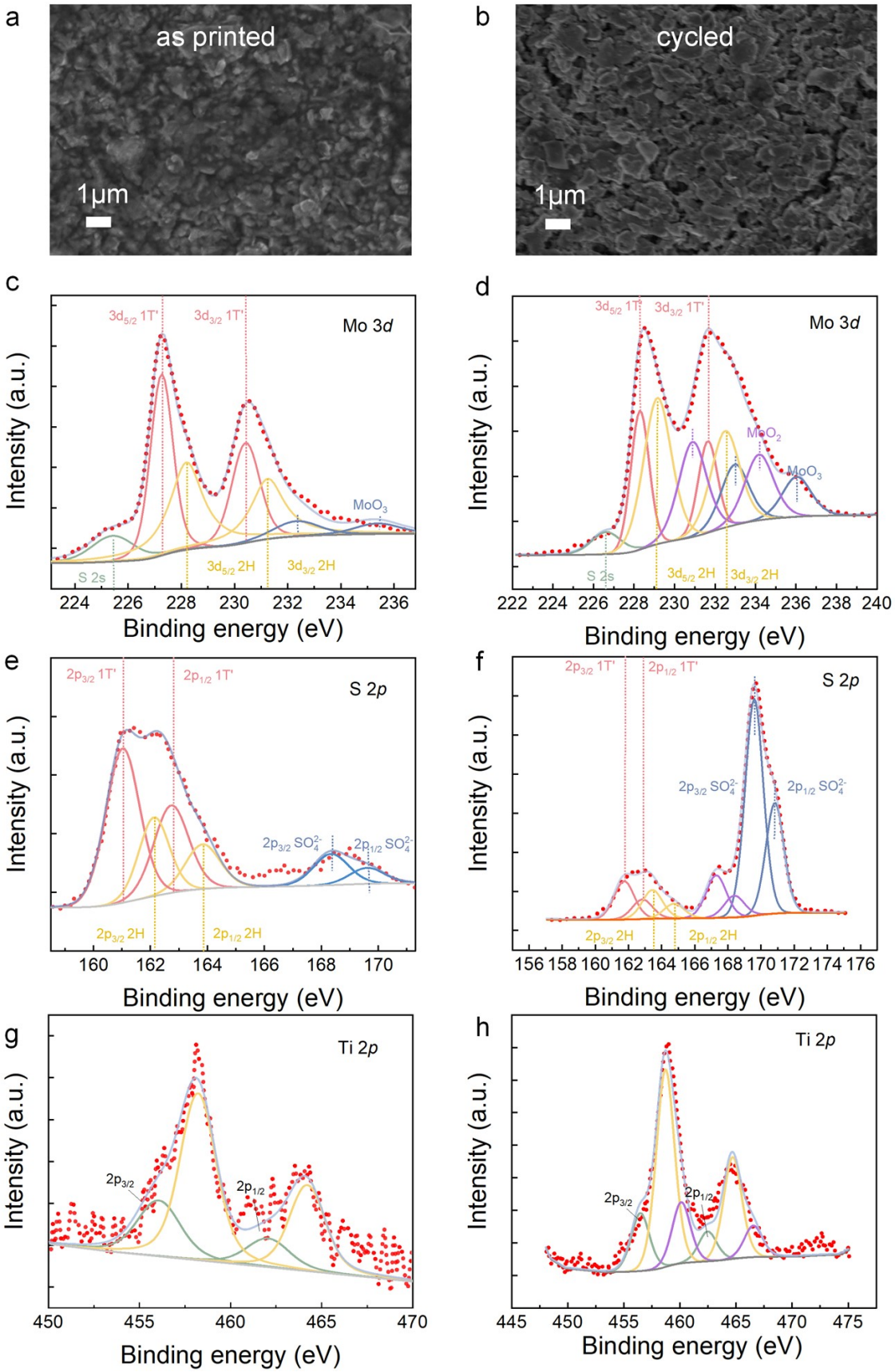

Figure S2. a) SEM Images of as printed samples and b) cycled samples in 1M H_2SO_4. c) The Mo 3d core level of as printed samples showing the doublet centred at 227.3 eV and 230.4 eV

(pink line) assigned to the 1T' MoS_2 (Mo 4^+)), while the doublet at 228.2 eV and 231.2 eV (yellow line) to the 2H MoS_2 (Mo 4^+)[5]. A negligible doublet of Mo 3d 5/2 and 3/2 centred at 232.32 eV and 235.37eV (dark blue line) is identified and is ascribable to Mo-O bonds (Mo 6^+), which is likely to be present at the edges of the flakes[6–8]. The peak at 225.4 eV is due to the S 2s core level (green line). A smart background was subtracted. d) The same region recorded for the sample cycled in 1M H_2SO_4. e) The S 2p core level of as printed samples showing the doublet located at 161.04 eV and 162.14 eV (pink line) assigned to the 1T' phase of MoS_2 (S^{2-}), however this doublet may also have a contribution from the S^{2-} in 1T TiS_2 (this doublet appears at 160.9 and 162.1 eV and can't be resolved). The doublet centred at 162.73 eV and 163.83 eV (yellow colour line) is ascribed to 2H phase of MoS_2 (S^{2-})[1]. A smart background was subtracted. The doublet at 168.34 eV and 169.61 eV can be attributed to sulphur in metal sulphate due to oxidation[9]. f) The same region for cycled samples in 1M H_2SO_4. The purple line shows a contribution from crystalised electrolyte components or by-products that arise after cycling. g) The Ti 2p core levels of as printed samples showing the doublet of the Ti 2p3/2 and p1/2 at 456.1 eV and 462.1 eV (green line) respectively that are assigned to the Ti^{4+} from TiS_2, while the doublet at 458.2 eV and 464.2 eV (yellow line) to the Ti^{4+} from TiO_2[10]. A smart background was subtracted. h) The same region recorded for the sample cycled in 1M H_2SO_4. The additional purple doublet is assigned to the TiO_x/Ti species.

Figure S3. a) XPS survey of as printed samples and b) XPS survey of cycled samples in 1M H_2SO_4.

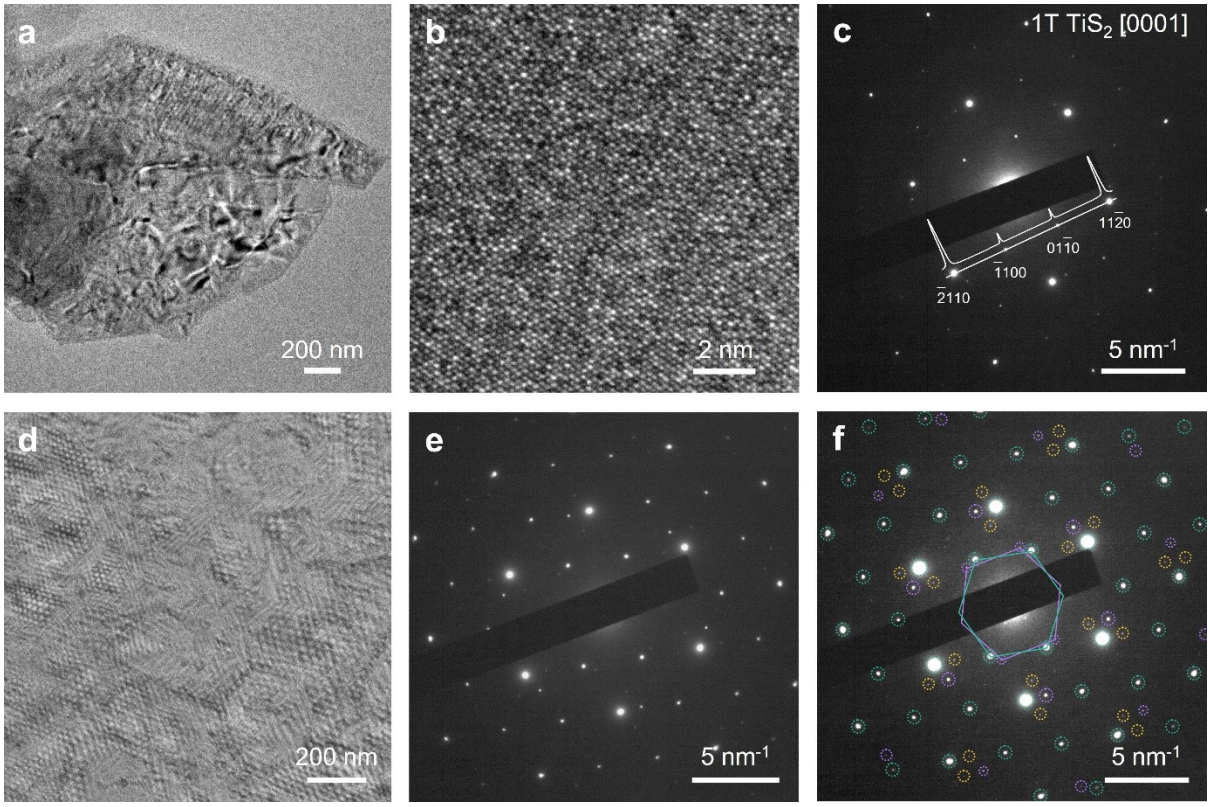

Figure S4. (a) Low-magnification TEM image of exfoliated TiS_2 flake. (b) High-resolution TEM image illustrating high crystallinity of the exfoliated material. (c) A representative SAED pattern of exfoliated TiS_2. The intensity profile in SAED pattern in panel b demonstrates the relative intensities of {100} and {110} diffraction spots characteristic to the 1T crystal phase of TiS_2. (d) Moiré patterns seen twisted bi- or few-layer 1T TiS_2 flakes. (e) Experimental SAED pattern of a twisted bi- or few-layer 1T TiS_2, shown in panel d, with evident PLD superstructure. (f) The same SAED with the markup that shows two sets of Bragg reflections of individual 1T TiS_2 domains (teal and purple circles) with the twist angle of ~12° and the PLD superstructure (yellow circles).

In low twist angle bi- (or few-) layer materials, a restructuring of moiré lattice occurs[11–13] . In addition to the two sets of Bragg reflections from individual layers, the periodic lattice displacements in twisted bilayers give rise to prominent satellite peaks. In panel f, two sets of 1T TiS_2 Bragg reflections are highlighted with teal and purple open circles, the PLD superstructure peaks, decorating the {110} and {300} Bragg peaks, are highlighted with yellow circles.

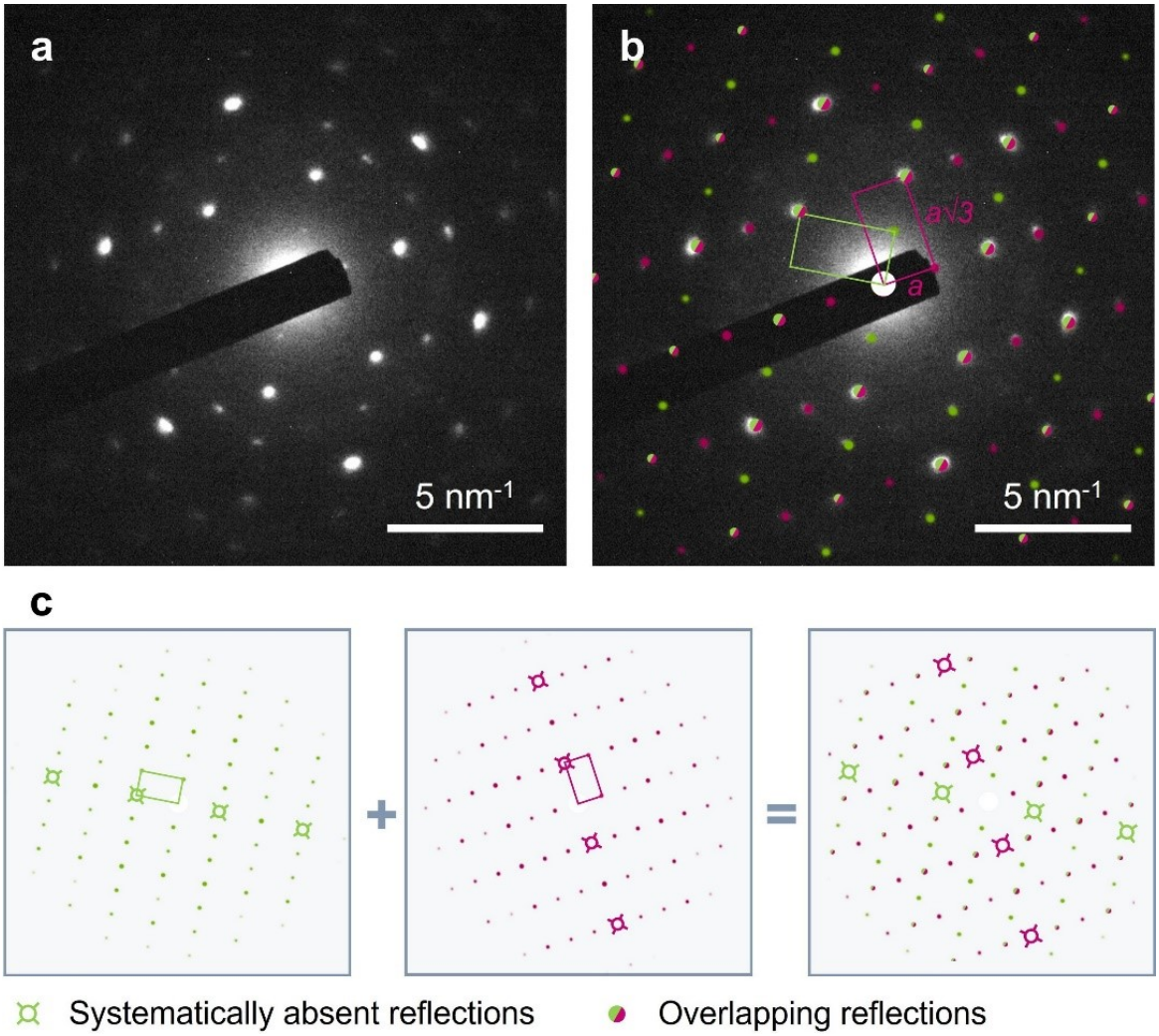

Figure S5. a) A representative experimental SAED pattern of exfoliated few-layer MoS_2. b) The experimental SAED pattern with the simulated diffraction pattern of a 1T' MoS_2 "twin" overlaid. c) A schematic showing the formation of a 1T' MoS_2 "twin" superstructure as an effect of superposition of Bragg reflections of two 1T' MoS_2 domains rotated by 120°.

The presence of characteristic zigzag chains of Mo atoms in the 1T' phases ($MoTe_2$, MoS_2) cause the crystal symmetry lowering to monoclinic[14]. This results in $a\sqrt{3}\times a$ diffraction spots arrays in diffraction patterns of pristine 1T' phase domains[1,15,16]. According to the selection rules, only the $0k0$ with k = 2n are allowed in the $P2_1/m$ 1T' MoS_2 crystals. This leads to systematic absence of ($0k0$) reflections with k = 2n + 1 in diffraction patterns of pristine 1T' MoS_2 as shown in panel c. A 1T' MoS_2 "twin" is formed by two 1T' MoS_2 domains rotated by 120°, and in SAED patterns taken along the [001] zone axis a "twin" appears as two superimposed $a\sqrt{3}\times a$ lattices as illustrated in panel c [17]. The simulated diffraction of a 1T' MoS_2 "twin" is in good agreement with the experimental observations (panel b). In contrast, the ordering of entrapped Li^+ cations in either 2H or 1T MoS_2 crystals is reported to manifest as uniform $2a\times 2a$ superlattices[4,18,19] that are not found in experimental SAED patterns of exfoliated MoS_2. This supports our interpretation that the superstructure observed in the experimental SAED of exfoliated few-layer MoS_2 originates from the "twins" of 1T' MoS_2 single layers rotated by 120°.

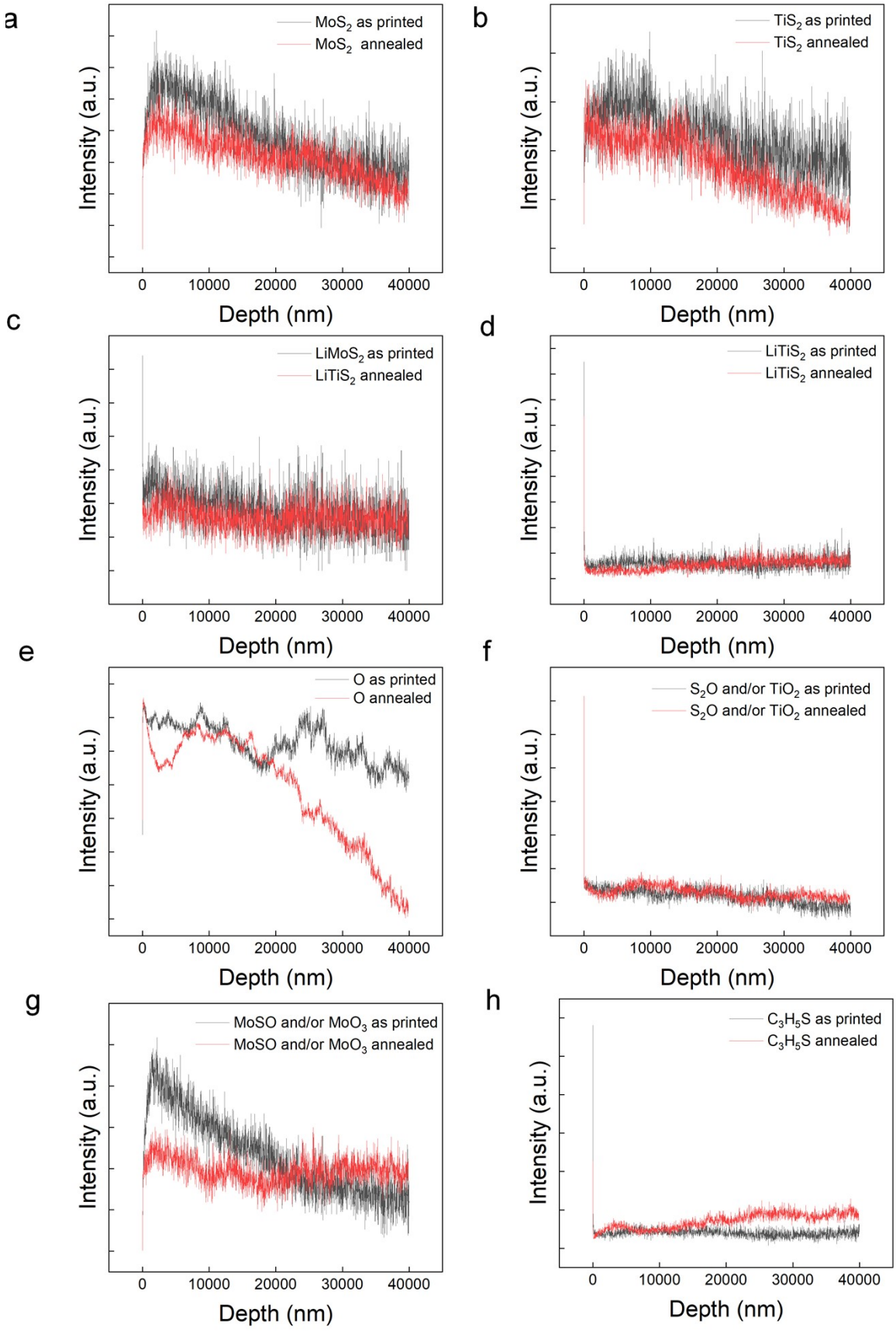
a
MoS2 as printed
MoS2 annealed
Intensity (a.u.)
0
10000
20000
30000
40000
Depth (nm)
b
TiS2 as printed
TiS2 annealed
Intensity (a.u.)
Depth (nm)
c
LiMoS2 as printed
LiTiS2 annealed
Intensity (a.u.)
Depth (nm)
d
LiTiS2 as printed
LiTiS2 annealed
Intensity (a.u.)
Depth (nm)
e
O as printed
O annealed
Intensity (a.u.)
Depth (nm)
f
S2O and/or TiO2 as printed
S2O and/or TiO2 annealed
Intensity (a.u.)
Depth (nm)
g
MoSO and/or MoO3 as printed
MoSO and/or MoO3 annealed
Intensity (a.u.)
Depth (nm)
h
C3H5S as printed
C3H5S annealed
Intensity (a.u.)
Depth (nm)

Figure S6. ToF-SIMS depth profiles of different ionic species present in as printed (black) and annealed (red) 3D serpentine structures. a) MoS_2 b) TiS_2 c) $LiMoS_2$ d) $LiTiS_2$ e) O f) S_2O which has the same mass as TiO_2 g) MoSO which has the same mass as MoO_3 and h) C_3H_5S

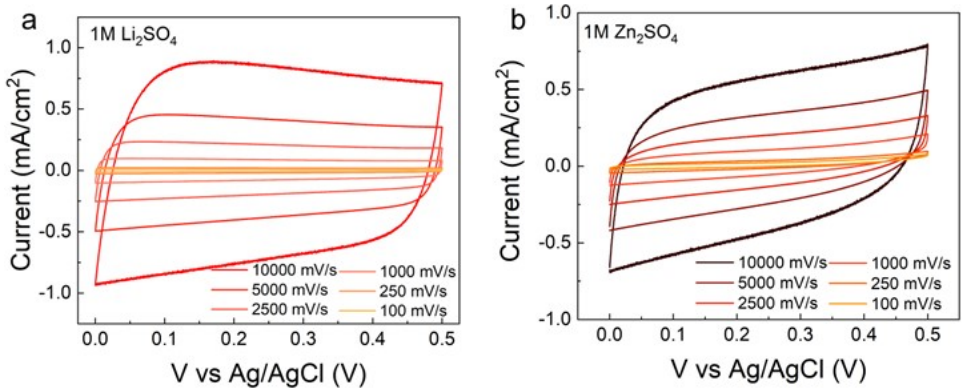

Figure S7. CV curves of 2 layered 50%wt MoS_2/TiS_2 annealed Serpentine structures in a) 1M Li_2SO_4 and b) 1M Zn_2SO_4 aqueous electrolytes across different scan rates in a three-electrode system with a Ag/AgCl reference electrode and a carbon foil ($1\times1cm^2$) counter electrode.

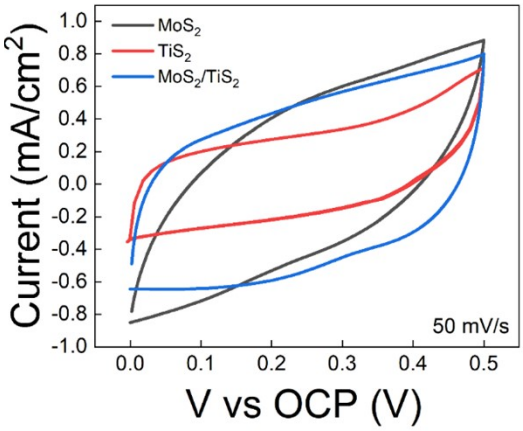

Figure S8. CV curves of symmetric devices of 50%wt MoS_2, 50%wt TiS_2 and 50%wt MoS_2/TiS_2 composite blends (50:50 molar ratio) in a 50:50 molar ratio at a constant 50 mV s^{-1} scan rate.

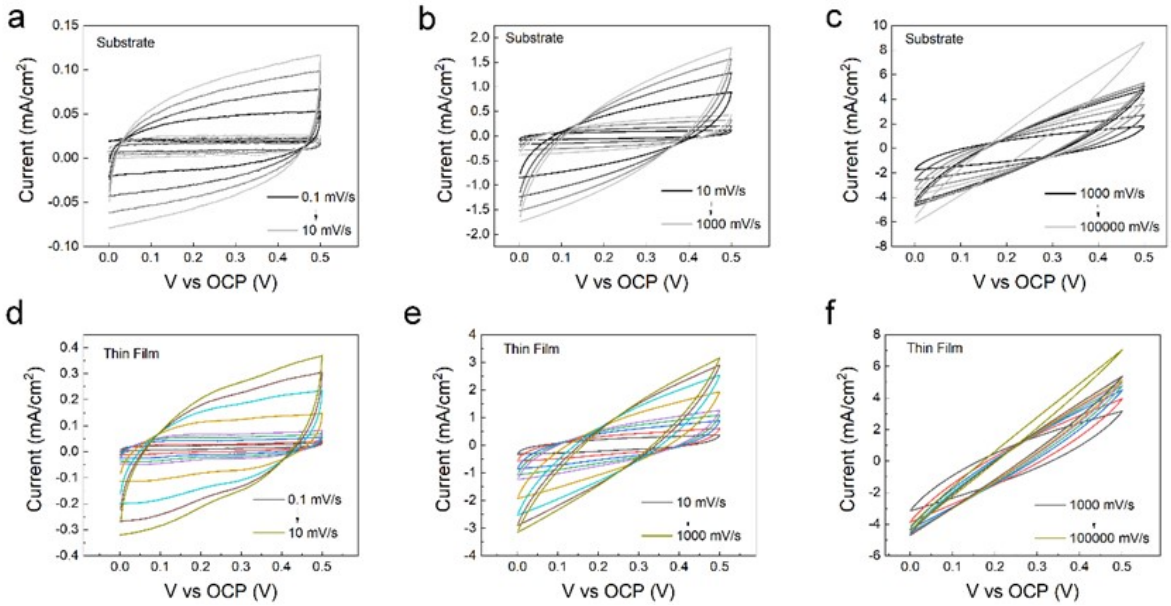

Figure S9. a)-c) CVs of bare substrates and d), e), f) 50%wt MoS_2/TiS_2 thin films across a),d) 0.1- 10mV/s b), e) 10-1,000mV/s and c),f) 1,000-10,000 mV/s scan rates.

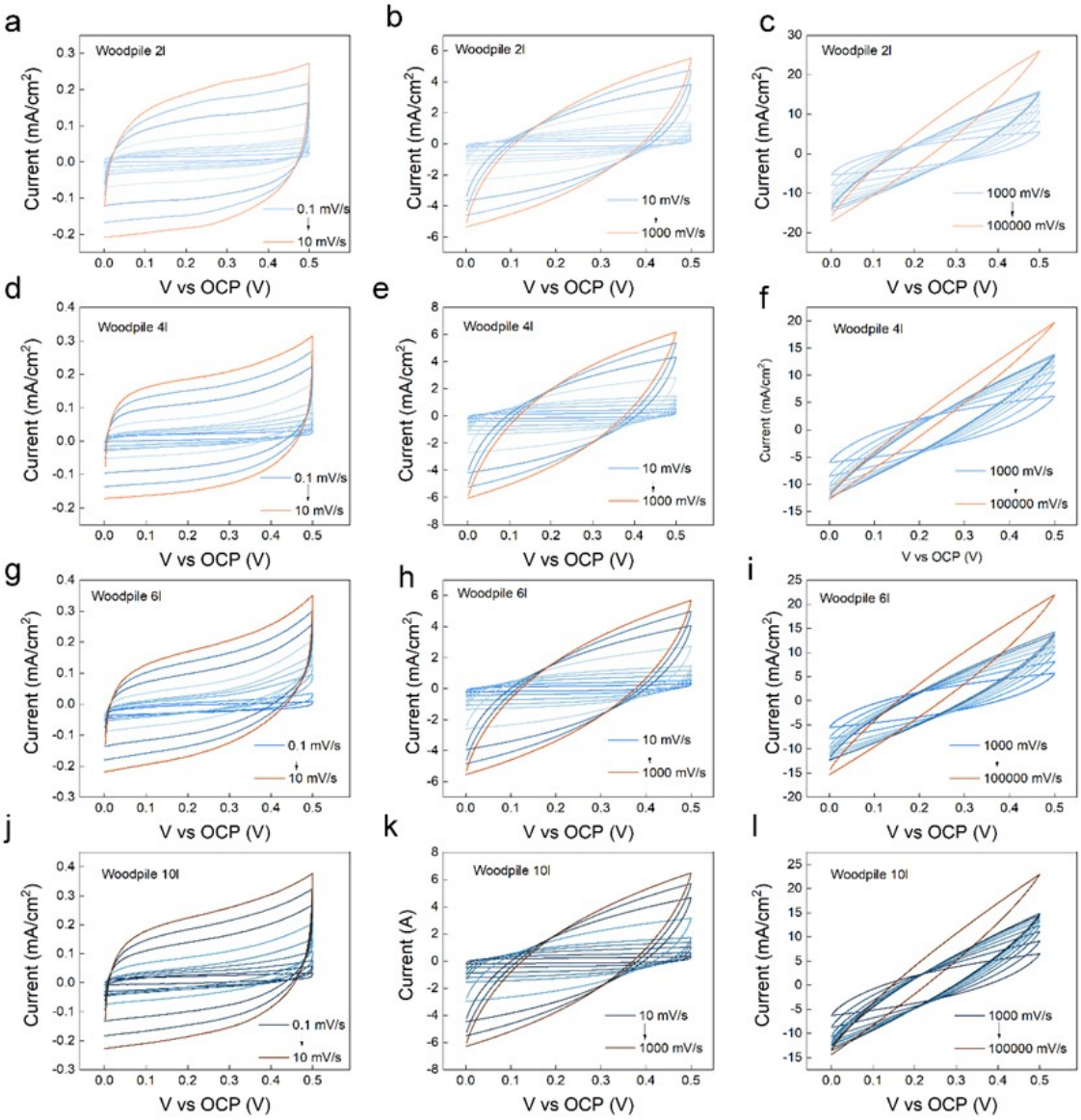

Figure S10. CVs of woodpile structures formed by a)b)c) 2, d),e),f) 4, g)h)i)6 and j)k)l)10 layers across a)d)g)k)0.1-10 mV/s b)e)h)k)10- 1,000 mV/s and c)f)i)l) ,1000-10,000 scan rates.

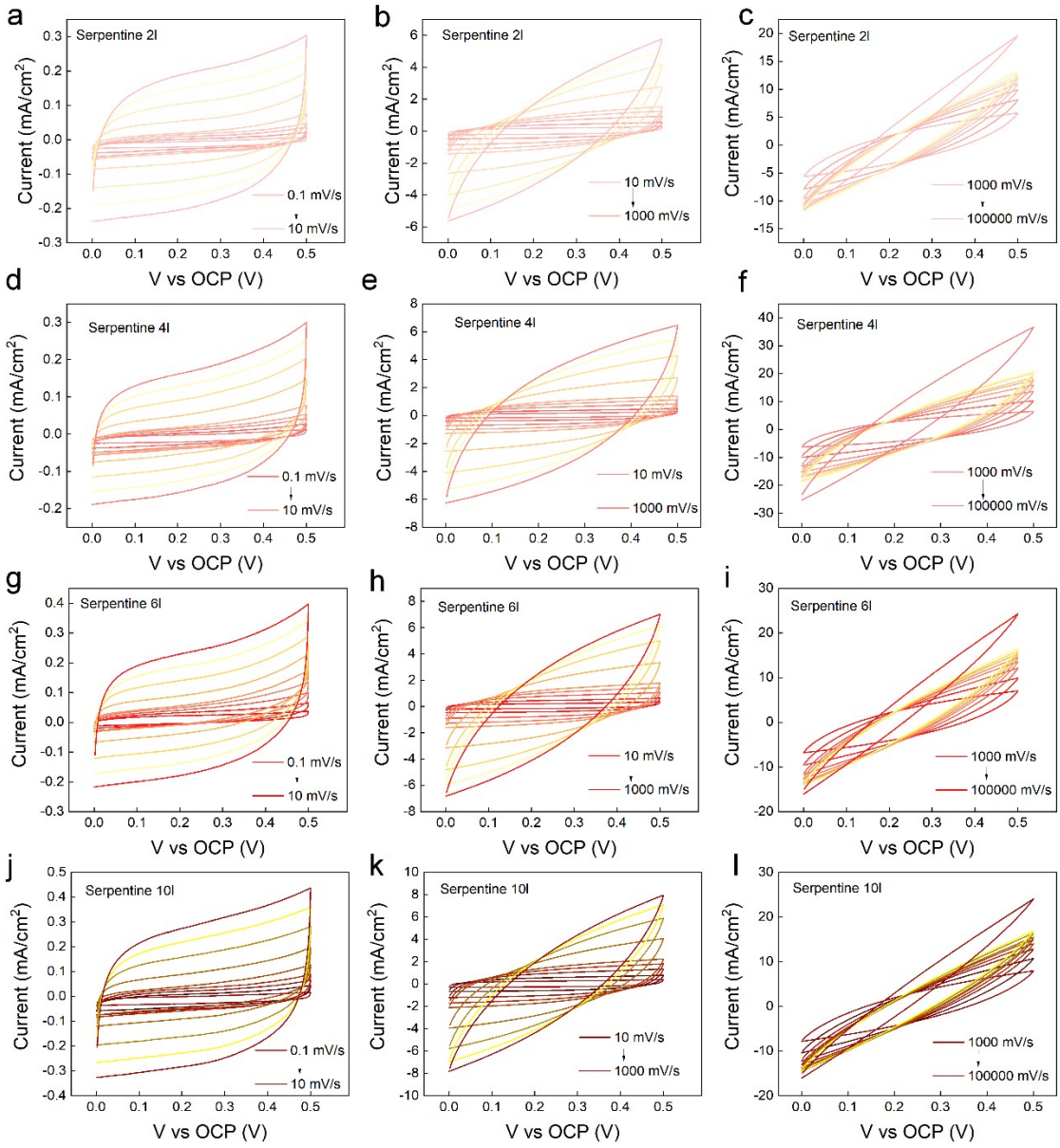

Figure S11. CVs of serpentine structures formed by a)b)c)2, d),e),f)4, g)h)i)6 and j)k)l)10 layers across a)d)g)k)0.1-10 mV/s b)e)h)k)10- 1,000 mV/s and c)f)i)l) ,1000-10,000 scan rates.

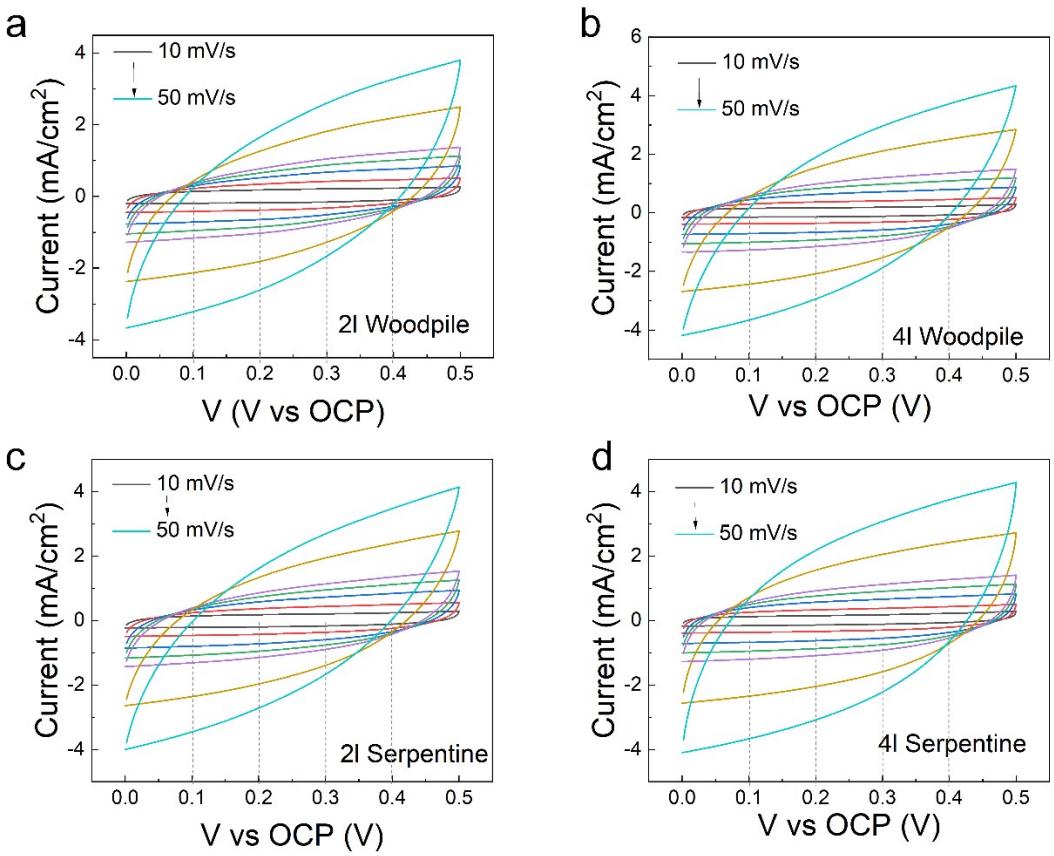

Figure S12. CVs used for capacitance contribution studies. a) 2l Woodpile, b) 4l Woodpile c) 2l Serpentine and d)4l Serpentine

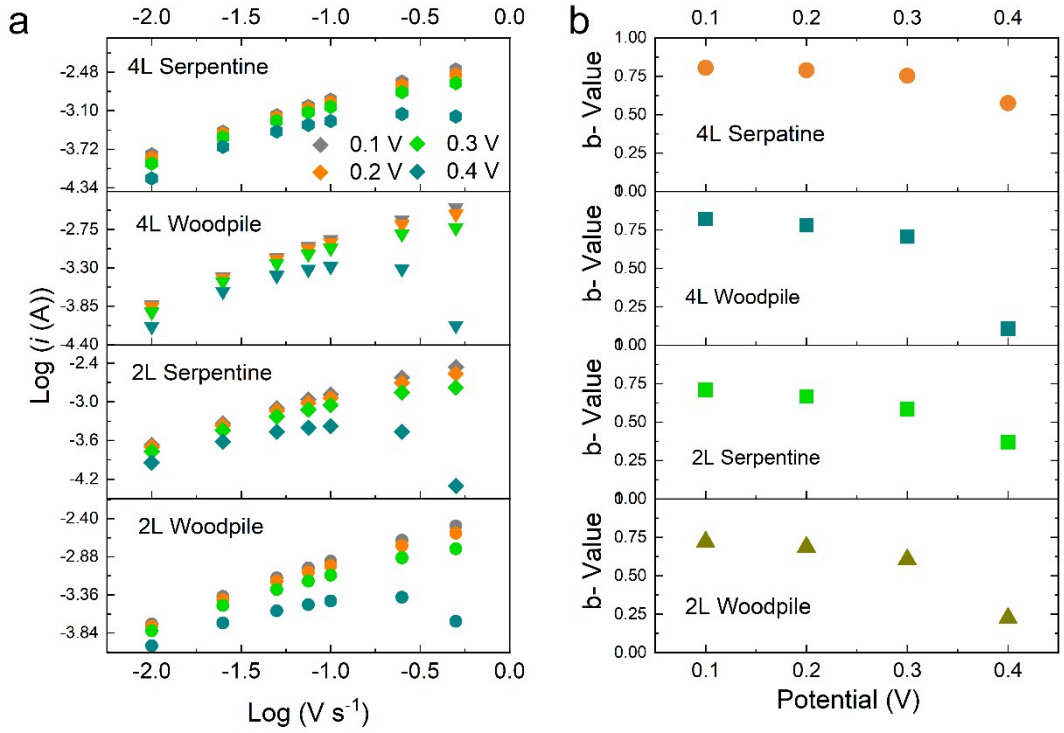

Figure S13. b-Values for capacitance contribution studies. a) Current logarithms and b) b-values of 2l-4l Woodpile and 2l-4l Serpentine structures.

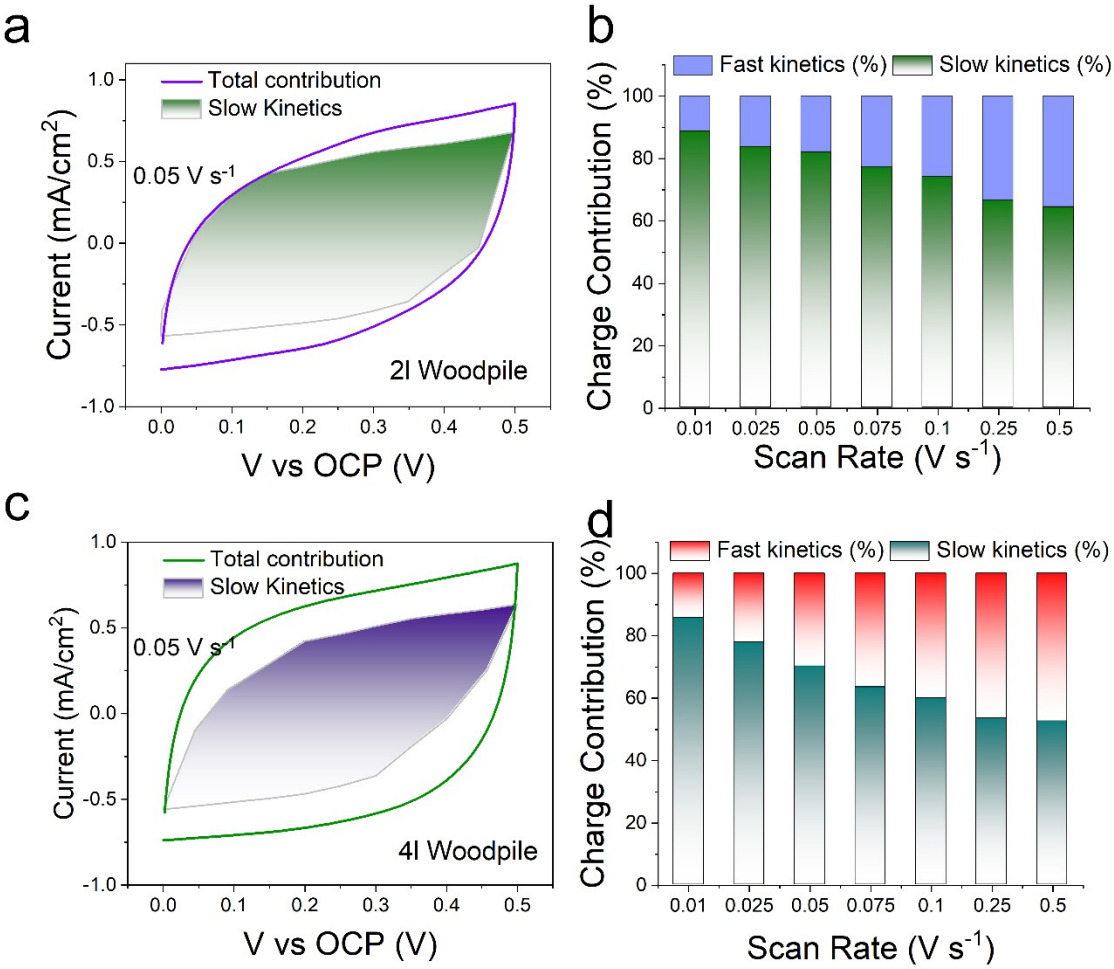

Figure S14. a) Capacitance contribution and b) kinetics of 2layered Woodpile structure. c)Capacitance contribution and d) kinetics in 4l woodpile structure.

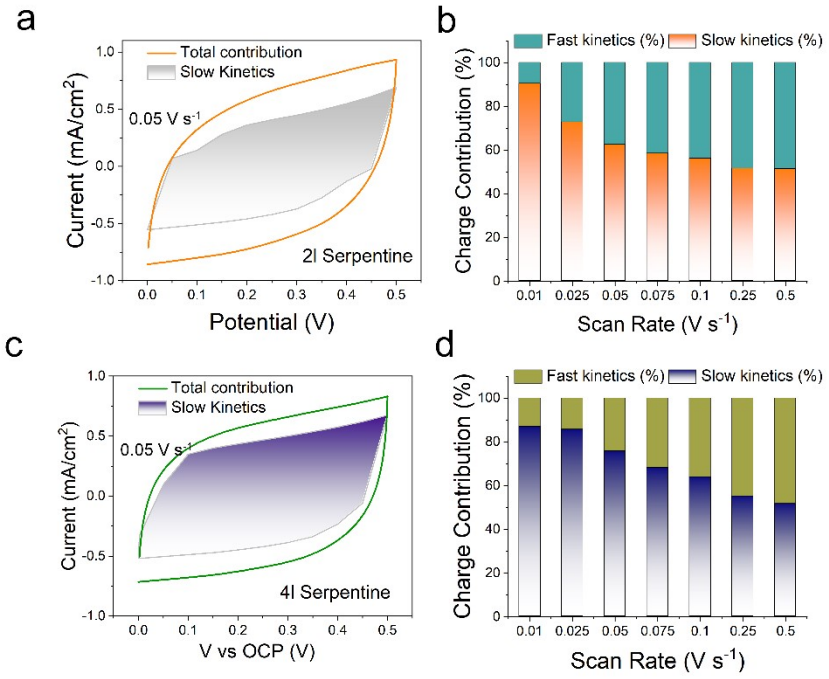

Figure S15. a) Capacitance contribution and b) kinetics of 2layered Serpentine structure. c)Capacitance contribution and d) kinetics in 4l Serpentine structure.

Chronoamperometric integration.
Charges are directly integrated from the current that is generated at a fixed potential over the time that is applied.

$$Q = \int_{t_0}^{t_1} i(t)dt \ \#Eq\ S1$$

t_0 = Time where potential is applied, t_1= Time where potential is stopped being applied. i(t)= current that is applied at a fixed potential over time.

$$C = \frac{Q}{V} \#Eq\ S2$$

Capacitance in coulometric studies is calculated from the charges as extracted from controlled potential coulometry over the fixed potential that is applied.

Cyclic Voltammetry integration
Charges were also extracted from CVs of devices using the below formula

$$Q = \oint \frac{i}{2v} dV \ \#EqS3$$

Capacitance values by integrating the area from CV using the below formula

$$Cdev = 4 * \frac{\oint i\, dV}{2\, v\, \Delta V\, x} \#Eq\ S4$$

Where ΔV is the voltage window (0.5V), v the scanrate, x is the area of the device immersed in the electrolyte, i is the current

Power-law and reformulated Power-law
Power-law and modified Power-law were utilized, as presented in Fig. S13, S14, S15, S16

In general, the Power-law can be conveyed as

$$i_p = a \times v^b \ \#Eq\ S5$$

Where i_p is the peak current (A), a is a constant, v the scanrate and b is the Power-law exponent. The b values from CV curves were calculated using the slope of a linear fit to the plot of log$v$ vs. log(i_p). When the b value is approximately 1, it signifies that the material follows capacitive electrochemical behaviour, while the diffusion-controlled charge storage behaviour is dominant when the value is ~0.5.
The percentage values of both the capacitive-controlled and diffusion-controlled processes were calibrated using the reformulated Power-Law, as shown below.

$$i_p = k_1 v + k_2 v^{\frac{1}{2}} \#Eq\ S6$$

$$i_p / v^{\frac{1}{2}} = k_1 v^{\frac{1}{2}} + k_2 v \#Eq\ S7$$

Here, i_p is the peak current, v scanrate and k_1, k_2 are constants.

By plotting the linear fit of $i/v^{1/2}$ vs, $v^{1/2}$, the slope and intercept values of k_1 and k_2 can be obtained. Thus, the portion of capacitive and diffusion-controlled contributions during the redox process were calculated using Eq S7.

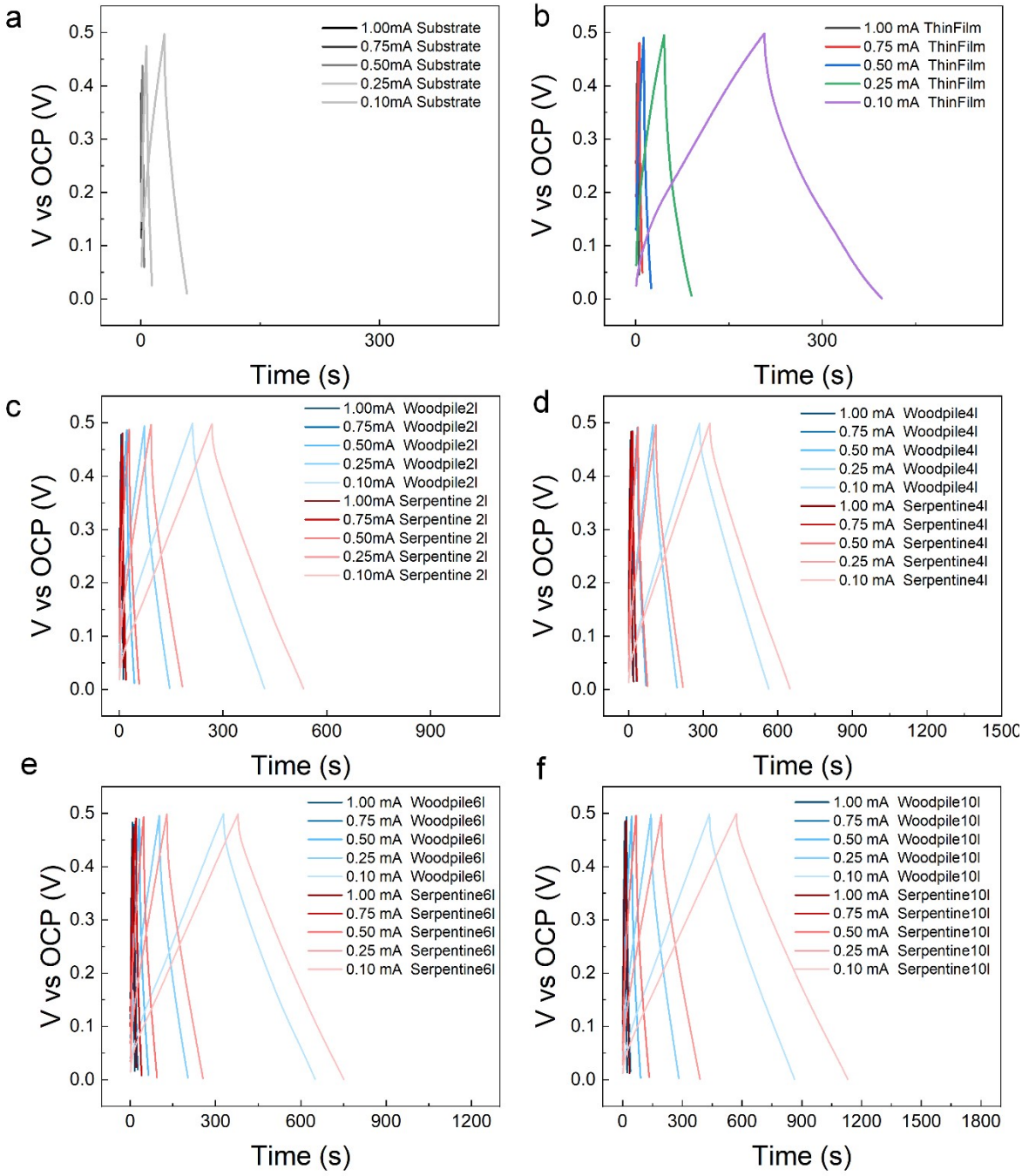

Figure S16. a) CCDs of the substrate, in 1-0.1mA/cm^2 Current Densities. b) CCDs of the 50% wt. MoS_2/TiS_2 thin films, in 1-0.1mA/cm^2 current densities. c)d)e)f)50% wt. MoS_2/TiS_2

architectures in c)2, d)4, e)6 and f) 10 layers of woodpile and serpentine structures at 1-0.1 mA/cm^2 current densities.

Cyclic Charge Discharge

Capacitance was calculated from symmetric devices using the below formula

$$C = 4\frac{I * \Delta t}{x * DV} \#Eq\ S8$$

Where I is the discharge current, Δt is the discharging time. X is the area of the device immersed in the electrolyte or the weight of the active material and DV is the discharge potential window.

Energy Density was calculated from symmetric devices using the below formula

$$E = \frac{1}{8} * \frac{C * DV^2}{3600} \#Eq\ S9$$

Where E is energy density, C is the capacitance calculated from CCD and DV is the discharge potential window.

Power Density was calculated from symmetric devices using the below formula

$$P = \frac{E}{\Delta t} \#Eq\ S10$$

Capacitance of devices was compared to the device CCD and Chronocoulometric device values by integrating the area from CV using the below formula

$$Cdev = 4 * \frac{\oint i\ dV}{2\ v\ \Delta V\ x} \#Eq\ S11$$

Where ΔV is the voltage window (0.5V), v the scanrate, x is the area of the device immersed in the electrolyte, i is the current

Charges were also extracted from CVs of devices using the below formula

$$Q = \oint \frac{i}{2v} dV \#Eq\ S12$$

All equations were used and formulated as expressed by Conway in 'Electrochemical supercapacitors'[20]. Adjustments were made between symmetric, to account for overestimations as expressed by Stoller and Ruoff[21] . Also, best practices and methods as expressed by Mathis et al, Simon et al and Lukatskaya et al [22–25], were considered.

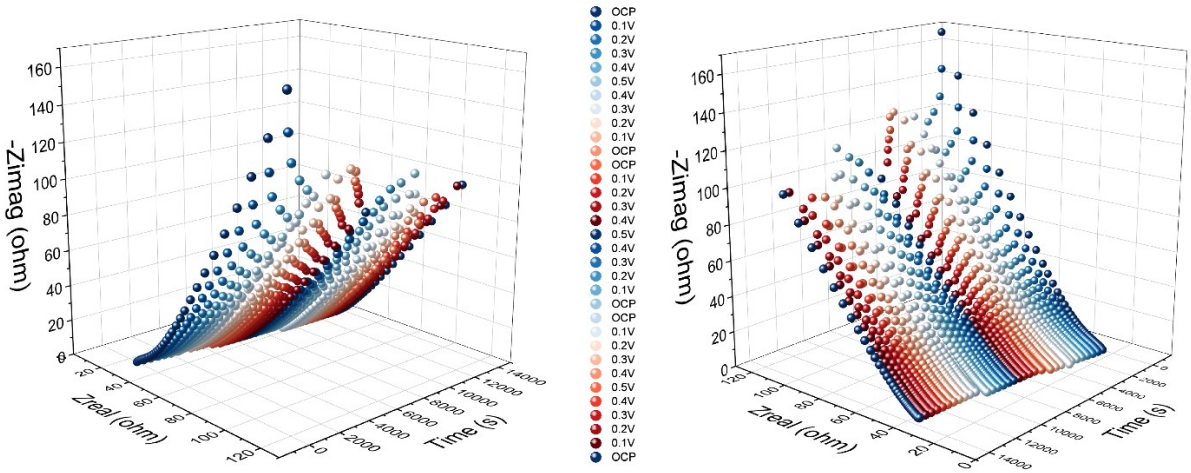

Figure S17. Stereoscopic figure of the effect of the potential window cycling and device ageing in a 2 layered serpentine structure.

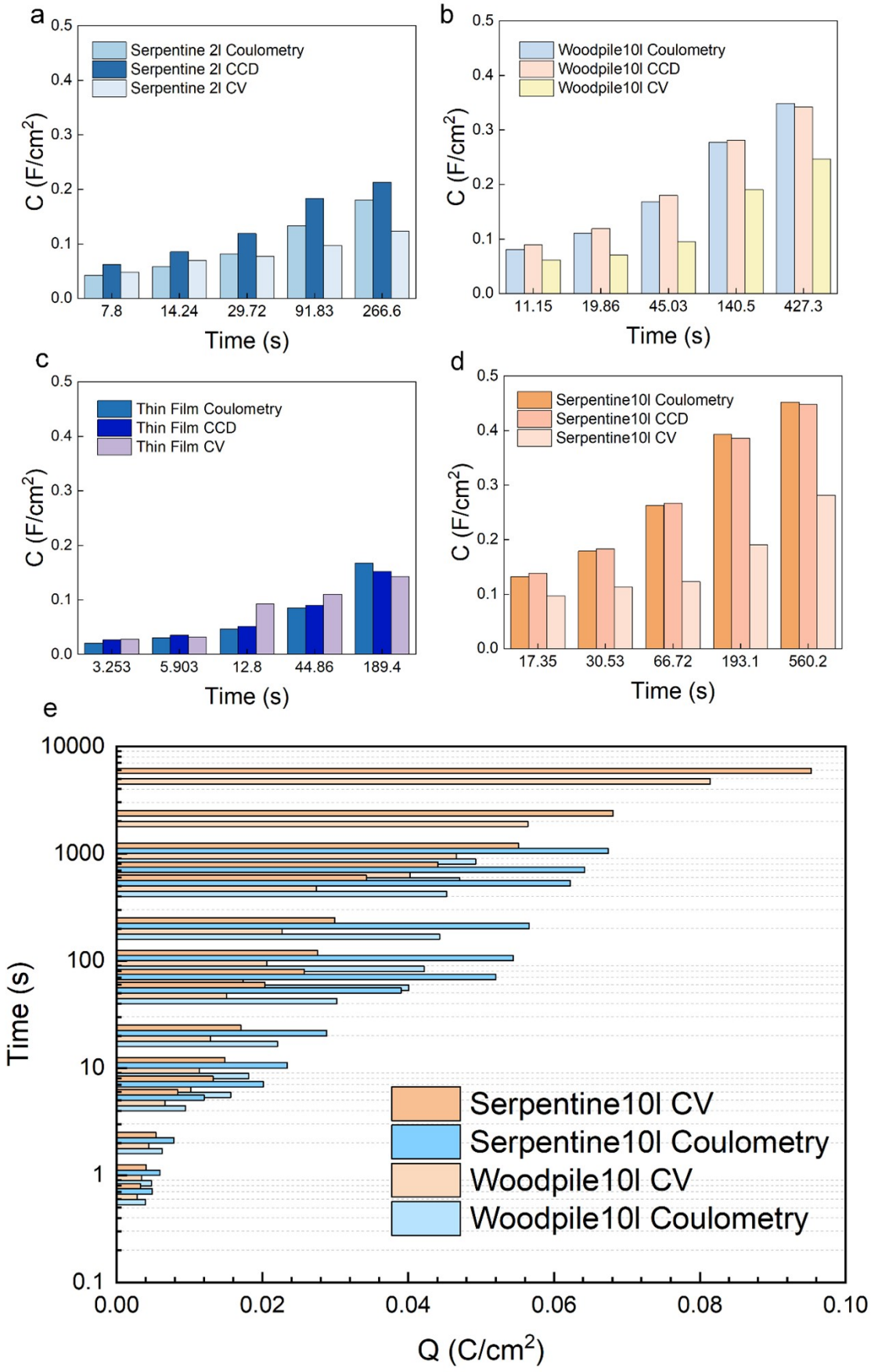

Figure S18. Capacitance comparison with values extracted from Cyclic Voltammetry, Coulometry and Cycling Charge Discharge in a)2layered Serpentine architecture, b)

10layered Woodpile Architecture c) Thin Film and d) 10layered Serpentine architecture. e) Charge storage comparison with values extracted from Cyclic Voltammetry and Coulometry in a 10layered Serpentine and 10layered Woodpile structure.

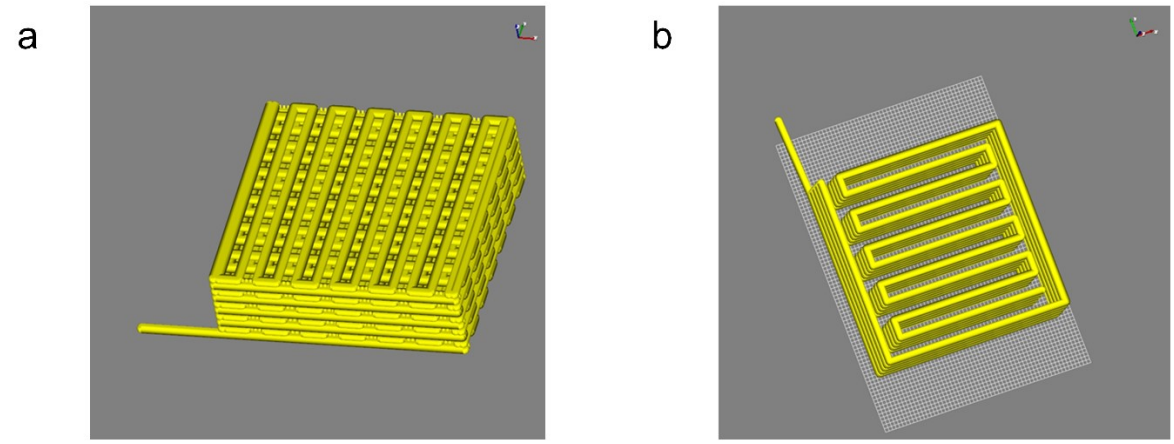

Figure S19. a) .CAD architecture of a 10layered Woodpile Structure. b) .CAD Architecture of a 10layered Serpentine Structure

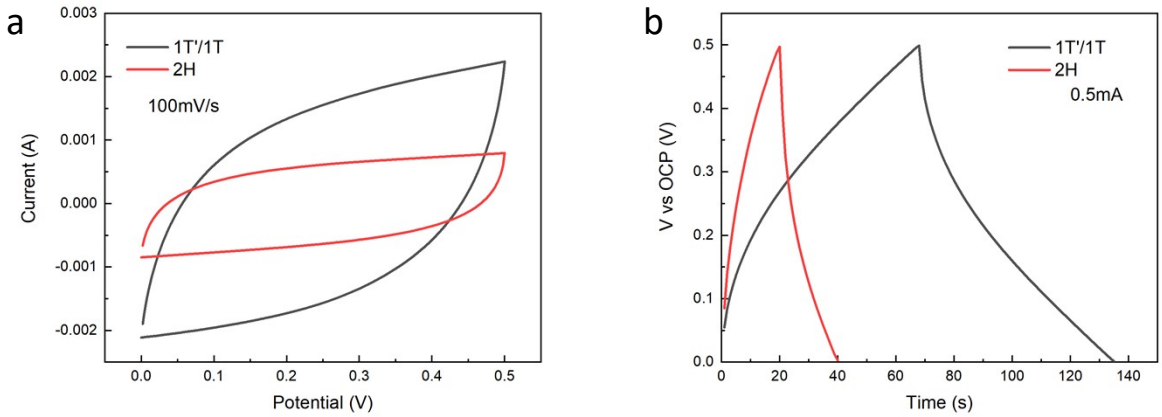

Figure S20. Comparative electrochemical properties of as printed 1T'/1T MoS_2/TiS_2 electrode and annealed (2H phase) electrodes. a) CV curves measured at a constant scan rate of 100 mV s^{-1} and charge-discharge curves obtained at constant current of 0.5 mA cm-2, demonstrating the higher capacitance properties for the printed 1T'/1T MoS_2/TiS_2 electrode.

As presented in the comparative CV and CD curves between the 1T'/1T and 2H phase of printed structures (Figure S20), higher integral current and charge-discharge response were observed in the 1T'/1T MoS_2/TiS_2, leading to a higher capacitance in the corresponding electrode. This could be mainly due to the increased electrical conductivity of 1T'/1T MoS_2/TiS_2 composite, which provides an improved transport of charges compared with the semiconducting 2H phase in the electrode architecture.

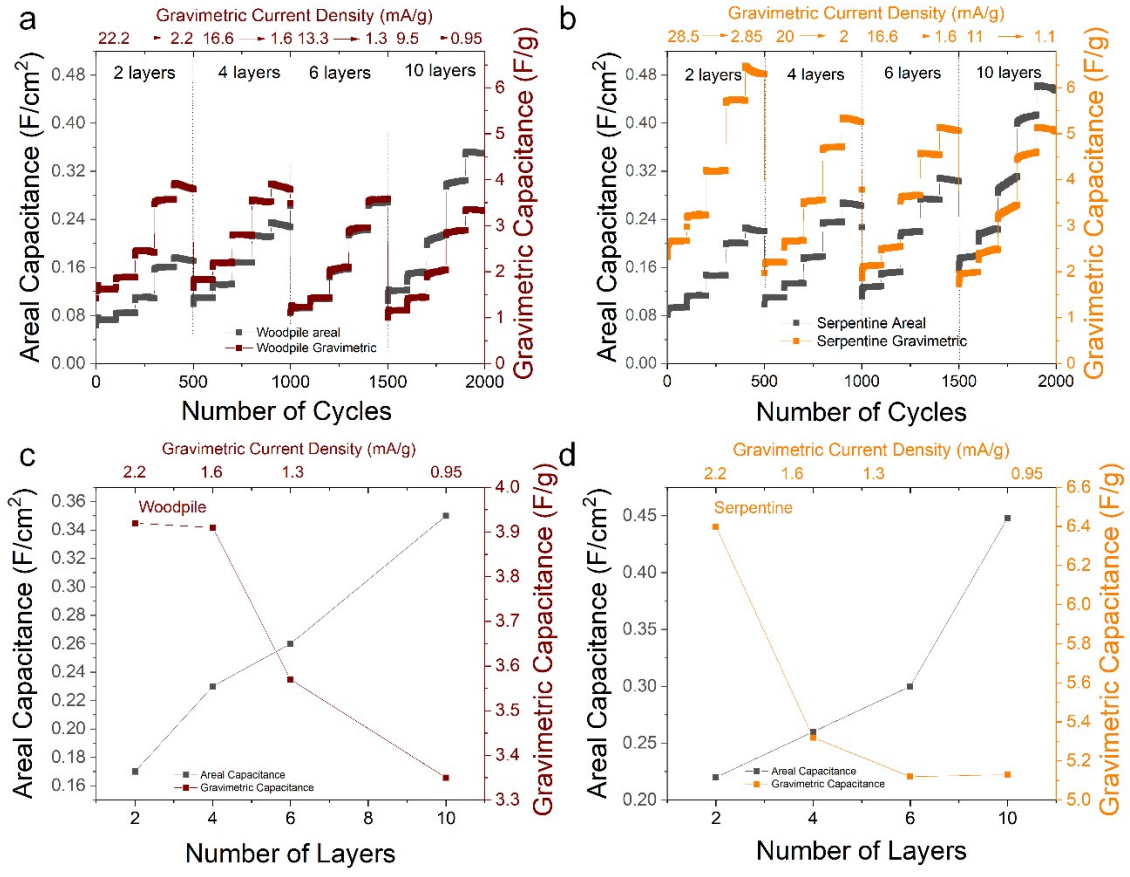

Figure S21 a)-c) areal capacitance versus gravimetric capacitance comparison during cycling charge discharge in 2-10 layered Woodpile architectures. b)-d) areal capacitance versus gravimetric capacitance comparison during cycling charge discharge in 2-10 layered serpentine architectures.

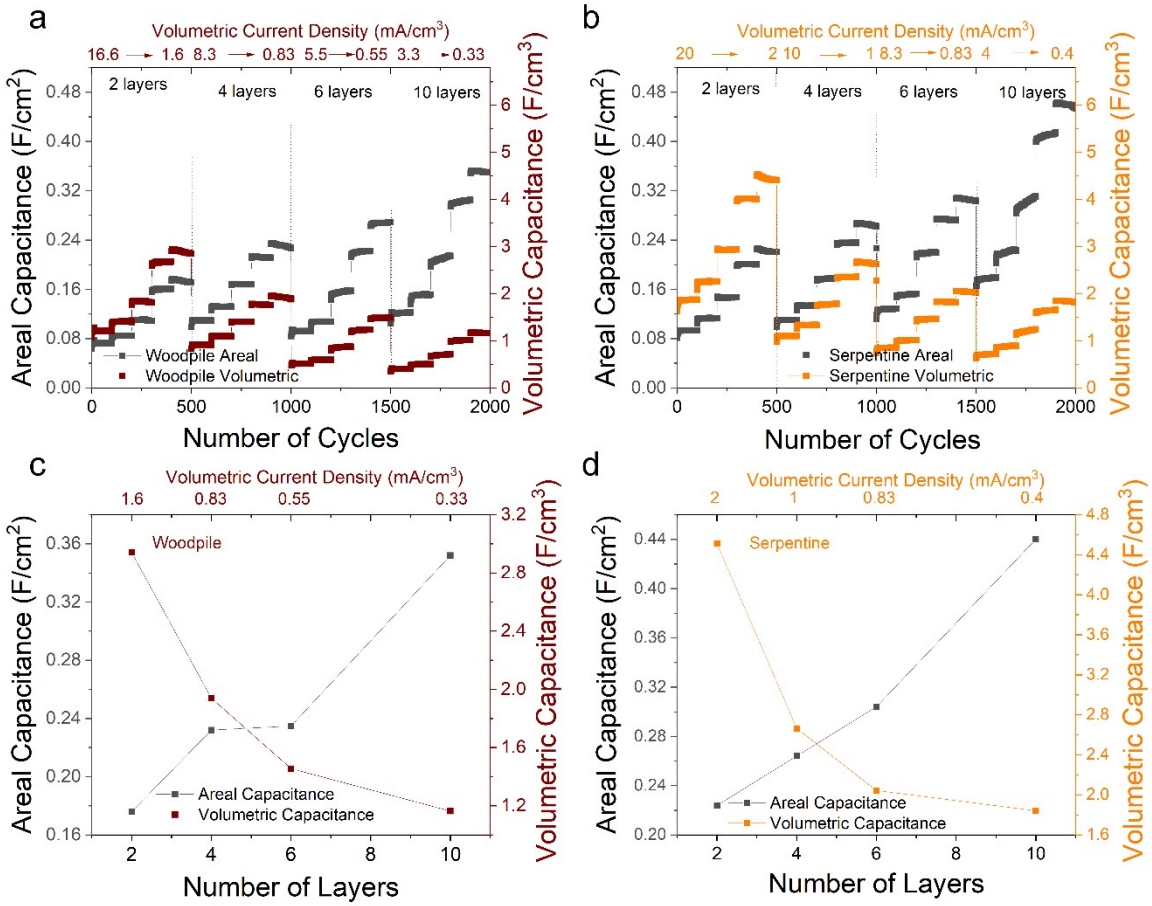

Figure S22 a)-c)Areal Capacitance versus volumetric capacitance comparison during cycling charge discharge in 2-10 layered woodpile architectures. b)-d) areal capacitance versus volumetric capacitance comparison during cycling charge discharge in 2-10 layered serpentine architectures.

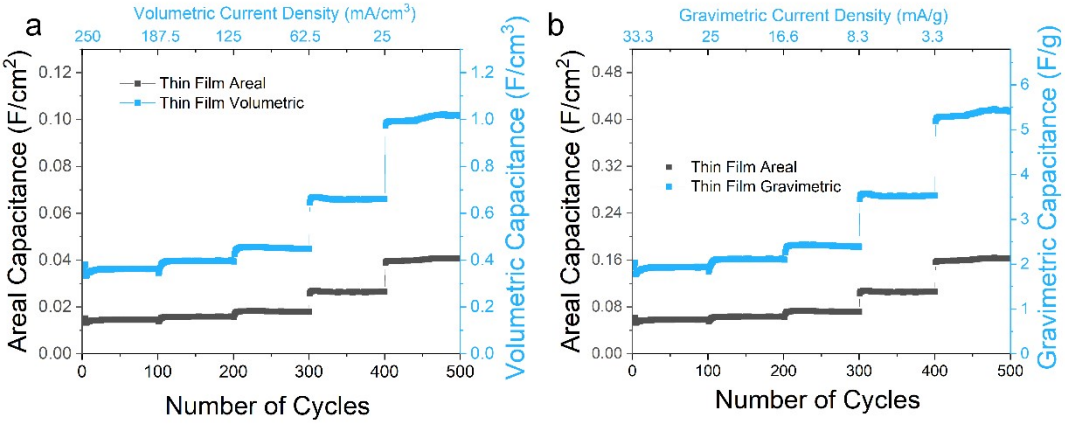

Figure S23 a) Areal Capacitance versus volumetric capacitance comparison during cycling charge discharge in 50%wt MoS_2/TiS_2 ink 1×1cm thin films b) areal capacitance versus gravimetric capacitance comparison during cycling charge-discharge in 50%wt MoS_2/TiS_2 ink 1×1 cm thin film.

Table S1. Comparison of areal energy and power densities reported in recent literature for TMDs – based supercapacitors assembled with unscalable manufacturing methods.

Material	Power Density (W/cm^2)	Energy Density (Wh/cm^2)	Ref
MoS_2/TiS_2 Woodpile	2.50E-04 1.88E-04 1.25E-04 6.25E-05 2.50E-05	7.74E-07 1.03E-06 1.56E-06 2.44E-06 2.97E-06	This Work
MoS_2/TiS_2 Serpentine	2.50E-04 1.88E-04 1.25E-04 6.25E-05 2.50E-05	1.20E-06 1.59E-06 2.32E-06 3.35E-06 3.89E-06	This Work
MoS_2/CNTs (3el)	1.50E-04 2.00E-04 2.50E-04	2.50E-06 2.22E-06 6.94E-07	50(Main Text)[26]
1T/2H MoS_2/Gr	5.00E-05 1.50E-04 2.00E-04 2.50E-04	1.67E-06 9.17E-07 9.44E-07 6.94E-07	51(Main Text)[27]
MoS_2/Graphene	2.00E-05 3.50E-05 4.00E-05 4.50E-05	1.44E-06 9.72E-07 6.67E-07 3.75E-07	52(Main Text)[28]
MoS_2/PEDOT/CNTs	1.60E-05 2.40E-05 3.20E-05 4.00E-05 8.00E-05	1.20E-06 8.00E-07 4.44E-07 2.78E-07 1.56E-07	53(Main Text)[29]
MoS_2/Graphite on Steel	5.00E-06 1.00E-05 2.00E-05 3.00E-05 4.00E-05	6.25E-07 5.56E-07 3.89E-07 3.75E-07 3.89E-07	54(Main Text) [30]
Laser Induced Graphene (3el)	6.25E-05	5.21E-08	55(Main Text)[31]
Laser Induced Graphene/ MoS_2 (3el)	6.25E-05	2.95E-07	55(Main Text)[31]
VS_4 on Cu	1.20E-05 1.80E-05 2.40E-05 3.60E-05 4.20E-05	2.67E-07 1.50E-07 1.67E-07 1.50E-07 1.17E-07	56(Main Text)[32]
MXene on Cu	1.20E-05 1.80E-05 2.40E-05 3.00E-05 3.60E-05 4.20E-05	1.90E-07 1.25E-07 6.00E-08 5.83E-08 5.00E-08 3.50E-08	56(Main Text)[32]
WS_2 nanowire (3el)	5.00E-05 1.00E-04 1.50E-04	2.78E-07 1.39E-07 1.25E-07	57(Main Text)[33]

	2.00E-04	1.11E-07	
MoS_2 (3el)	2.00E-04	1.67E-07	58(Main Text)[34]
$MoSe_2$ (3el)	2.00E-04	6.67E-08	58(Main Text)[34]
$MoTe_2$ (3el)	2.00E-04	2.78E-08	58(Main Text)[34]
MoS_2 inkjet printed	6.00E-07 1.20E-06 1.80E-06 2.40E-06	1.50E-08 1.00E-08 1.00E-08 1.00E-08	59(Main Text)[35]

TABLE S2. Active material mass loadings and volumetric areas for each electrode tested.

Layers	Serpentine Mass Loading (g)	Serpentine Volumetric Area (cm^3)	Woodpile Mass Loading (g)	Woodpile Volumetric Area (cm^3)
2	0.035	1x1x0.05	0.035	1x1x0.06
4	0.05	1x1x0.1	0.06	1x1x0.012
6	0.06	1x1x0.15	0.075	1x1x0.18
10	0.09	1x1x0.25	0.105	1x1x0.3
Thin Film	0.013 g	1x1x0.004		

SI References

1. Heising, J. & Kanatzidis, M. G. Structure of restacked MoS_2 and WS_2 elucidated by electron crystallography. *J Am Chem Soc* **121**, 638–643 (1999).
2. Voiry, D. *et al.* Conducting MoS2 nanosheets as catalysts for hydrogen evolution reaction. *Nano Lett* **13**, 6222–6227 (2013).
3. Suslov, E. A., Bushkova, O. V., Sherstobitova, E. A., Reznitskikh, O. G. & Titov, A. N. Lithium intercalation into TiS2 cathode material: phase equilibria in a Li–TiS_2 system. *Ionics (Kiel)* **22**, 503–514 (2016).
4. Heising, J. & Kanatzidis, M. G. Exfoliated and restacked MoS_2 and WS_2: Ionic or neutral species? Encapsulation and ordering of hard electropositive cations. *J Am Chem Soc* **121**, 11720–11732 (1999).
5. Eda, G. *et al.* Photoluminescence from chemically exfoliated MoS2. *Nano Lett* **11**, 5111–5116 (2011).
6. Cattelan, M. *et al.* New Strategy for the Growth of Complex Heterostructures Based on Different 2D Materials. *Chemistry of Materials* **27**, 4105–4113 (2015).
7. Martinez, H. *et al.* Influence of the cation nature of high sulfur content oxysulfide thin films MOySz (M=W, Ti) studied by XPS. *Appl Surf Sci* **236**, 377–386 (2004).
8. Dupin, J. C., Gonbeau, D., Benqlilou-Moudden, H., Vinatier, P. & Levasseur, A. XPS analysis of new lithium cobalt oxide thin-films before and after lithium deintercalation. *Thin Solid Films* **384**, 23–32 (2001).
9. Moulder, J. F., Chastain, Jill. & King, R. C. Handbook of x-ray photoelectron spectroscopy : a reference book of standard spectra for identification and interpretation of XPS data. 261 (1995).
10. Huckaba, A. J. *et al.* Low-Cost TiS_2 as Hole-Transport Material for Perovskite Solar Cells. *Small Methods* **1**, 1700250 (2017).
11. Sung, S. H. *et al.* Torsional periodic lattice distortions and diffraction of twisted 2D materials. *Nature Communications 2022 13:1* **13**, 1–8 (2022).
12. Hovden, R. *et al.* Atomic lattice disorder in charge-density-wave phases of exfoliated dichalcogenides (1T-TaS2). *Proc Natl Acad Sci U S A* **113**, 11420–11424 (2016).
13. Mannix, A. J. *et al.* Robotic four-dimensional pixel assembly of van der Waals solids. *Nature Nanotechnology 2022 17:4* **17**, 361–366 (2022).
14. Keum, D. H. *et al.* Bandgap opening in few-layered monoclinic $MoTe_2$. *Nature Physics 2014 11:6* **11**, 482–486 (2015).
15. Nam, G.-H. *et al.* In-Plane Anisotropic Properties of 1T'-MoS_2 Layers. *Advanced Materials* **31**, 1807764 (2019).
16. Guo, C. *et al.* Observation of superconductivity in 1T'-MoS_2 nanosheets. *J Mater Chem C Mater* **5**, 10855–10860 (2017).
17. Amara, K. K. *et al.* Dynamic Structural Evolution of Metal-Metal Bonding Network in Monolayer WS2. *Chemistry of Materials* **28**, 2308–2314 (2016).
18. Huang, Q. *et al.* The Mechanistic Insights into the 2H-1T Phase Transition of MoS_2 upon Alkali Metal Intercalation: From the Study of Dynamic Sodiation Processes of MoS2 Nanosheets. *Adv Mater Interfaces* **4**, 1700171 (2017).
19. Tan, S. J. R. *et al.* Chemical Stabilization of 1T' Phase Transition Metal Dichalcogenides with Giant Optical Kerr Nonlinearity. *J Am Chem Soc* **139**, 2504–2511 (2017).
20. Conway, B. E. Electrochemical Supercapacitors. *Electrochemical Supercapacitors* (1999) doi:10.1007/978-1-4757-3058-6.

21. Stoller, M. D. & Ruoff, R. S. Best practice methods for determining an electrode material's performance for ultracapacitors. *Energy and Environmental Science* vol. 3 1294–1301 Preprint at https://doi.org/10.1039/c0ee00074d (2010).
22. Mathis, T. S. *et al.* Energy Storage Data Reporting in Perspective—Guidelines for Interpreting the Performance of Electrochemical Energy Storage Systems. *Adv Energy Mater* **9**, 1902007 (2019).
23. Simon, P. & Gogotsi, Y. Materials for electrochemical capacitors. *Nat. Mater.* **7**, 845–854 (2008).
24. Lukatskaya, M. R., Dunn, B. & Gogotsi, Y. Multidimensional materials and device architectures for future hybrid energy storage. *Nature Communications 2016 7:1* **7**, 1–13 (2016).
25. Simon, P. & Gogotsi, Y. Perspectives for electrochemical capacitors and related devices. *Nature Materials 2020 19:11* **19**, 1151–1163 (2020).
26. Tiwari, P., Jaiswal, J. & Chandra, R. Hierarchal growth of MoS2@CNT heterostructure for all solid state symmetric supercapacitor: Insights into the surface science and storage mechanism. *Electrochim Acta* **324**, 134767 (2019).
27. Zhang, C. *et al.* Hybridized 1T/2H-MoS_2/graphene fishnet tube for high-performance on-chip integrated micro-systems comprising supercapacitors and gas sensors. *Nano Research 2020 14:1* **14**, 114–121 (2020).
28. Zhao, J., Gao, L., Wang, Z., Wang, S. & Xu, R. Boosting the performance of flexible in-plane micro-supercapacitors by engineering MoS_2 nanoparticles embedded in laser-induced graphene. *J Alloys Compd* **887**, 161514 (2021).
29. Wang, Q., Liang, X., Zhang, D. & Miao, M. A multifunctional supercapacitor based on 2D nanosheets on a flexible carbon nanotube film. *Dalton Transactions* **49**, 9312–9321 (2020).
30. Mohammed, M. M. M. & Chun, D. M. All-Solid-State Supercapacitor Based on MoS2–Graphite Composite Prepared by the Vacuum Kinetic Spray Method. *Journal of Thermal Spray Technology* **28**, 963–973 (2019).
31. Clerici, F. *et al.* In situ MoS_2 Decoration of Laser-Induced Graphene as Flexible Supercapacitor Electrodes. *ACS Appl Mater Interfaces* **8**, 10459–10465 (2016).
32. Sharma, A. *et al.* All-solid-state asymmetric supercapacitors based on VS4 nano-bundles and MXene nanosheets. *J Mater Sci* **56**, 20008–20025 (2021).
33. Choudhary, N. *et al.* High-Performance One-Body Core/Shell Nanowire Supercapacitor Enabled by Conformal Growth of Capacitive 2D WS2 Layers. *ACS Nano* **10**, 10726–10735 (2016).
34. Mukherjee, S. *et al.* Exfoliated transition metal dichalcogenide nanosheets for supercapacitor and sodium ion battery applications. *R Soc Open Sci* **6**, (2019).
35. Han, Z. *et al.* A Study of All-solid-state Planar Micro-supercapacitors Using Printable MoS2 Inks. *https://doi.org/10.1246/cl.200736* **50**, 452–455 (2020).